

Coherent structures and the saturation of a nonlinear dynamo

ERICO L. REMPEL^{1†}, ABRAHAM C.-L. CHIAN²
 AXEL BRANDENBURG^{3,4} AND PABLO R. MUÑOZ¹

¹Institute of Aeronautical Technology (ITA), World Institute for Space Environment Research (WISER), São José dos Campos – SP 12228–900, Brazil

²Observatoire de Paris, LESIA, CNRS, 92190 Meudon, France

³NORDITA, KTH Royal Institute of Technology and Stockholm University, Roslagstullsbacken 23, SE 10691 Stockholm, Sweden

⁴Department of Astronomy, Stockholm University, SE 10691 Stockholm, Sweden

(Received ?; revised ?; accepted ?. - To be entered by editorial office)

Eulerian and Lagrangian tools are used to detect coherent structures in the velocity and magnetic fields of a mean–field dynamo, produced by direct numerical simulations of the three–dimensional compressible magnetohydrodynamic equations with an isotropic helical forcing and moderate Reynolds number. Two distinct stages of the dynamo are studied, the kinematic stage, where a seed magnetic field undergoes exponential growth, and the saturated regime. It is shown that the Lagrangian analysis detects structures with greater detail, besides providing information on the chaotic mixing properties of the flow and the magnetic fields. The traditional way of detecting Lagrangian coherent structures using finite–time Lyapunov exponents is compared with a recently developed method called function M . The latter is shown to produce clearer pictures which readily permit the identification of hyperbolic regions in the magnetic field, where chaotic transport/dispersion of magnetic field lines is highly enhanced.

Key words: Lagrangian coherent structures, nonlinear dynamo, magnetohydrodynamics, chaotic mixing

1. Introduction

The description of chaotic and turbulent flows by means of embedded coherent structures is a topic of great interest in the study of transport and mixing in fluids, since these structures act as organizing units in the flow, defining attracting and repelling directions, transport barriers and regions of high or low dispersion of passive scalars. There is no standard way of defining what a coherent structure is, but from the Eulerian point of view, they are often defined based on some measure related to vorticity. An example is the highly popular Q –criterion, first introduced by Hunt *et al.* (1988) to identify vortex cores based on the difference between the rate of strain and vorticity. Some other criteria define coherent structures or vortices based on local pressure minima (Jeong & Hussain 1995) or on quantities involving the eigenvalues of the gradient tensor of the velocity field (Chong *et al.* 1990; Zhou *et al.* 1999; Chakraborty *et al.* 2005; Varun *et al.* 2008). From a Lagrangian point of view, coherent structures are seen as material surfaces that

† Email address for correspondence: rempel@ita.br

form the boundaries between regions of the flow with different behavior, such as vortex surfaces. They are found by following trajectories of fluid particles, while computing quantities such as the maximum rate of divergence of neighboring trajectories (Haller 2001; Shadden *et al.* 2005) or the arc-length of the trajectory (Madrid & Mancho 2009). Lagrangian tools are naturally suited for unsteady flows, since they take into account the temporal variations of the vector field, not just instantaneous snapshots. For a recent list of applications, see Peacock & Dabiri (2010).

Most works on Lagrangian coherent structures (LCSs) have focused on hydrodynamic turbulence, mainly in two-dimensions. A few papers have computed LCSs for three-dimensional magnetohydrodynamic (MHD) systems in the conservative (Leoncini *et al.* 2006) and dissipative (Rempel *et al.* 2011, 2012) regimes. In the aforementioned dissipative cases, only velocity field (kinetic) structures were explored. Here, we expand our previous results by computing the kinetic and magnetic coherent structures in a MHD model of mean-field dynamo. Dynamo action consists in the amplification of magnetic field by the motion of an electrically conducting fluid, being the mechanism responsible for the equipartition-strength magnetic fields observed in planets and stars (Brandenburg & Subramanian 2005). Initially, a weak magnetic field \mathbf{B} undergoes an exponential growth in the *kinematic dynamo* phase until \mathbf{B} is strong enough to impact the fluid velocity \mathbf{u} , and eventually the magnetic energy saturates. The saturation process is closely related to the suppression of Lagrangian chaos in the velocity field; a comparison between the chaoticity of the velocity field during the growth and saturation phases of the dynamo has been performed in previous works (Brandenburg *et al.* 1995; Cattaneo *et al.* 1996; Zienicke *et al.* 1998). In this paper, the emphasis is on the detection of coherent structures and the transport of passive scalars and magnetic field lines in the transition from the kinematic to the saturated phase. Eulerian structures are detected using the Q -criterion and, for the detection of LCSs, the traditional technique of finite-time Lyapunov exponents (FTLEs) is compared with the recently proposed function M (Madrid & Mancho 2009).

Section 2 of this paper describes the dynamo model adopted. The numerical results are presented in section 3, where the Eulerian and Lagrangian coherent structures are computed for the velocity and magnetic fields. Some conclusions are given in section 4.

2. The Model

The model is the prototype of α^2 dynamo used by Brandenburg (2001), where a compressible isothermal gas is considered, with constant sound speed c_s , constant dynamical viscosity μ , constant magnetic diffusivity η , and constant magnetic permeability μ_0 . The following set of compressible MHD equations is solved

$$\partial_t \ln \rho + \mathbf{u} \cdot \nabla \ln \rho + \nabla \cdot \mathbf{u} = 0, \quad (2.1)$$

$$\partial_t \mathbf{u} + \mathbf{u} \cdot \nabla \mathbf{u} = -\nabla p / \rho + \mathbf{J} \times \mathbf{B} / \rho + (\mu / \rho) (\nabla^2 \mathbf{u} + \nabla \nabla \cdot \mathbf{u} / 3) + \mathbf{f}, \quad (2.2)$$

$$\partial_t \mathbf{A} = \mathbf{u} \times \mathbf{B} - \eta \mu_0 \mathbf{J}, \quad (2.3)$$

where ρ is the density, \mathbf{u} is the fluid velocity, \mathbf{A} is the magnetic vector potential, $\mathbf{J} = \nabla \times \mathbf{B} / \mu_0$ is the current density, p is the pressure, \mathbf{f} is an external forcing, and $\nabla p / \rho = c_s^2 \nabla \ln \rho$, where $c_s^2 = \gamma p / \rho$ is assumed to be constant. Nondimensional units are adopted by setting $k_1 = c_s = \rho_0 = \mu_0 = 1$, where $\rho_0 = \langle \rho \rangle$ is the spatial average of ρ and k_1 is the smallest wavenumber in the box, which has sides $L = 2\pi$ and periodic boundary conditions. Thus, the time unit is $(c_s k_1)^{-1}$, space is measured in units of k_1^{-1} , \mathbf{u} in units

of c_s , \mathbf{B} in units of $(\mu_0\rho_0)^{1/2}c_s$, ρ in units of ρ_0 and the unit of viscosity $\nu \equiv \mu/\rho_0$ and magnetic diffusivity η is c_s/k_1 . Equations (2.1)–(2.3) are solved with the PENCIL CODE †, which employs an explicit sixth-order finite differences scheme in space and a third-order Runge–Kutta scheme for time integration.

The initial conditions are $\ln \rho = \mathbf{u} = 0$, and A is a set of normally distributed, uncorrelated random numbers with zero mean and standard deviation equal to 10^{-3} . The forcing function \mathbf{f} is given by

$$\mathbf{f}(\mathbf{x}, t) = \text{Re}\{N\mathbf{f}_{\mathbf{k}(t)} \exp[i\mathbf{k}(t) \cdot \mathbf{x} + i\phi(t)]\}, \quad (2.4)$$

where $\mathbf{k}(t) = (k_x, k_y, k_z)$ is a time-dependent wavevector, $\mathbf{x} = (x, y, z)$ is position, and $\phi(t)$ with $|\phi| < \pi$ is a random phase. On dimensional grounds the normalization factor is chosen to be $N = f_0 c_s (k c_s / \delta t)^{1/2}$, where f_0 is a nondimensional factor, $k = |\mathbf{k}|$, and δt is the length of the integration timestep. We focus on the case where $|\mathbf{k}|$ is around $k_f = 5$ and randomly select, at each timestep, one of 350 possible vectors in $4.5 < |\mathbf{k}| < 5.5$. The operator $\mathbf{f}_{\mathbf{k}}$ is given by

$$\mathbf{f}_{\mathbf{k}} = \frac{i\mathbf{k} \times (\mathbf{k} \times \mathbf{e}) - |\mathbf{k}|(\mathbf{k} \times \mathbf{e})}{k^2 \sqrt{2(1 - (\mathbf{k} \cdot \mathbf{e})^2)/k^2}}, \quad (2.5)$$

where \mathbf{e} is an arbitrary unit vector needed in order to generate a vector $\mathbf{k} \times \mathbf{e}$ that is perpendicular to \mathbf{k} . Note that $|\mathbf{f}_{\mathbf{k}}|^2 = 1$ and the helicity density satisfies $\mathbf{f} \cdot \nabla \times \mathbf{f} = |\mathbf{k}| \mathbf{f}^2 > 0$, which is an important condition for the production of a mean-field dynamo (Moffatt 1978). The forcing function is delta-correlated in time, i. e., all points of \mathbf{f} are correlated at any instant in time but are different at the next time step. Following Brandenburg (2001), the control parameters are set as $f_0 = 0.07$, $\nu = \eta = 0.002$ and the numerical resolution is 128^3 .

3. Results

3.1. Mean-field dynamo

Figure 1 shows the time series of $B_{rms} \equiv \langle B^2 \rangle^{1/2}$ (light line) and $u_{rms} \equiv \langle u^2 \rangle^{1/2}$ (dark line), where $B \equiv |\mathbf{B}|$ and $u \equiv |\mathbf{u}|$. During the first time units up to $t \sim 150$, the magnetic energy is too weak to significantly impact the velocity field and $u_{rms} \sim 0.28$, thus the Reynolds number is $Re = u_{rms}/\nu k_f \sim 28$. During this *kinematic phase*, B_{rms} increases exponentially, with a growth rate $\gamma \sim 0.064 \pm 2 \times 10^{-5}$ obtained from the fitted line (dashed line). After $t \sim 150$, u_{rms} starts to decay due to the contribution of the Lorentz force (second term in the right side of Eq. (2.2)). Eventually, the *r.m.s.* quantities saturate due to nonlinear effects, with $u_{rms} \sim 0.18$ while the magnetic field reaches a super-equipartition value $B_{rms} \sim 0.37 > u_{rms}$. The arrows indicate the times $t = 100$ and $t = 1700$, respectively, which will be used later to represent the kinematic and saturated phases. In turnover time units ($1/k_f u_{rms}$), the referred times are $u_{rms} k_f t \sim 140$ and $u_{rms} k_f t \sim 1530$, respectively, and the growth rate is $\gamma/u_{rms} k_f \sim 0.046$.

During the kinematic stage, the magnetic field displays low-amplitude stochastic fluctuations, as shown in the upper panels of Fig. 2. As B_{rms} grows, small-scale velocity and magnetic field fluctuations combine to produce a robust large-scale mean-field pattern (lower panels). The physics behind the rise of this mean-field is related to the so-called α -effect (Moffatt 1978) and has been explored in this model by Brandenburg (2001).

† <http://pencil-code.googlecode.com>

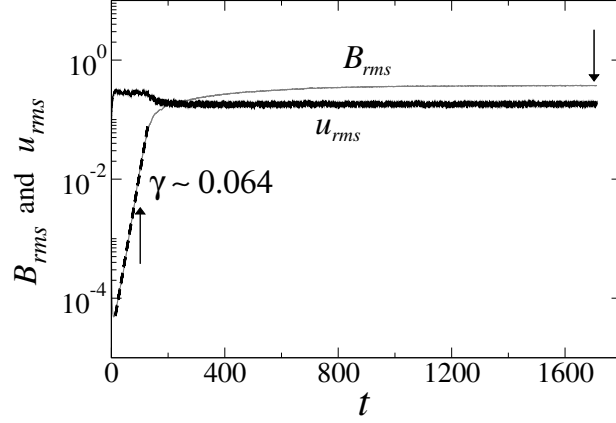
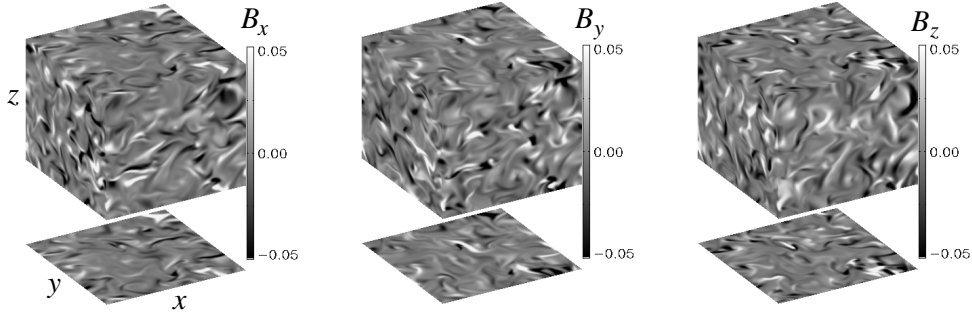


FIGURE 1. Time series of B_{rms} (light line) and u_{rms} (dark line) of MHD dynamo simulations for $\eta = \nu = 0.001$. The arrows indicate the kinematic phase at $t = 100$ and the saturated nonlinear regime at $t = 1700$, respectively. The growth rate during the kinematic phase is $\gamma \sim 0.064$.

a) $t = 100$



b) $t = 1700$

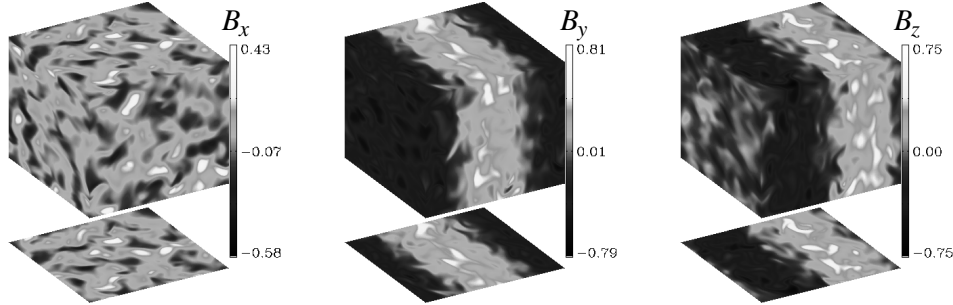


FIGURE 2. Intensity plot of magnetic field components at $t = 100$ (upper panel) and $t = 1700$ (lower panel).

3.2. Eulerian coherent structures

Eulerian coherent structures can be extracted from the velocity field by decomposing the gradient tensor $\nabla \mathbf{u}$ as

$$\nabla \mathbf{u} = \mathbf{S} + \mathbf{\Omega}, \quad (3.1)$$

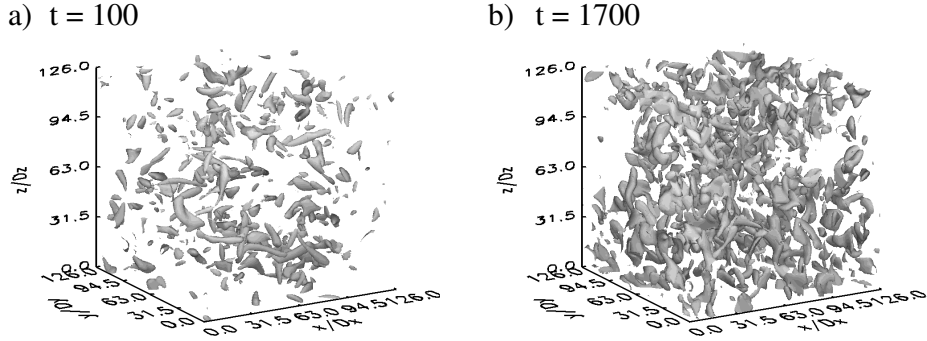


FIGURE 3. Eulerian coherent structures in the velocity field, detected by instantaneous isosurfaces of the Q -criterion. The isosurfaces are defined using 15% maximum Q .

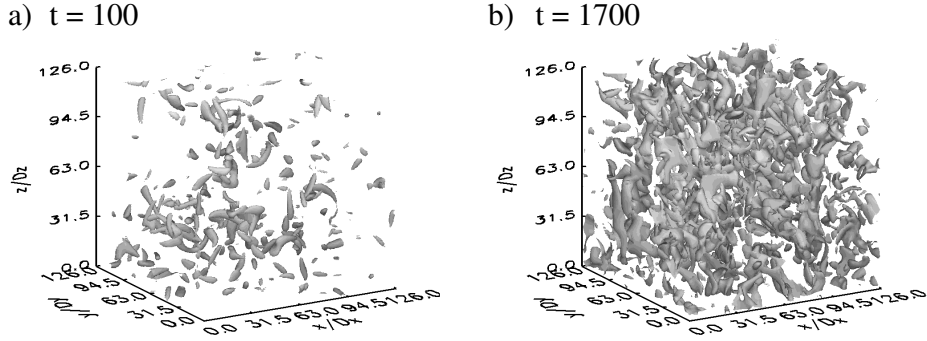


FIGURE 4. Eulerian coherent structures in the magnetic field, detected by isosurfaces of the Q -criterion. The isosurfaces are defined using 15% maximum Q .

where $\mathbf{S} = \frac{1}{2}[\nabla\mathbf{u} + (\nabla\mathbf{u})^T]$ and $\mathbf{\Omega} = \frac{1}{2}[\nabla\mathbf{u} - (\nabla\mathbf{u})^T]$ are the symmetric and antisymmetric parts of $\nabla\mathbf{u}$, respectively. The symmetric part is the rate-of-strain tensor and the antisymmetric part is the vorticity tensor. One way to define an Eulerian coherent structure is by finding regions of \mathbf{u} where vorticity dominates over strain, which can be measured by the Q -criterion (Hunt *et al.* 1988; Zhong *et al.* 1998; Haller 2005; Lawson & Barakos 2010)

$$Q = \frac{1}{2}[|\mathbf{\Omega}|^2 - |\mathbf{S}|^2]. \quad (3.2)$$

Thus, an Eulerian coherent structure or vortex is defined as a region where $Q > 0$.

Figure 3 shows the isosurfaces of the Q -criterion, using 15% maximum Q (contour surfaces enclose high Q values). These plots are highly dependent on the threshold chosen for Q , but it is possible to see that the fluid is more intermittent at the kinematic dynamo phase ($t = 100$) than after saturation ($t = 1700$), since in the right panel the coherent structures fill the space in a more homogeneous way. There are fewer regions for $t = 100$ where Q is much higher than the average, thus the presence of fewer vortices for this threshold in Fig. 3(a) than in 3(b), where local values of Q are closer to the average Q . Figure 4 shows the corresponding plots of Q for the magnetic field, where the coherent structures represent magnetic vortices or current structures Brandenburg *et al.* (1996).

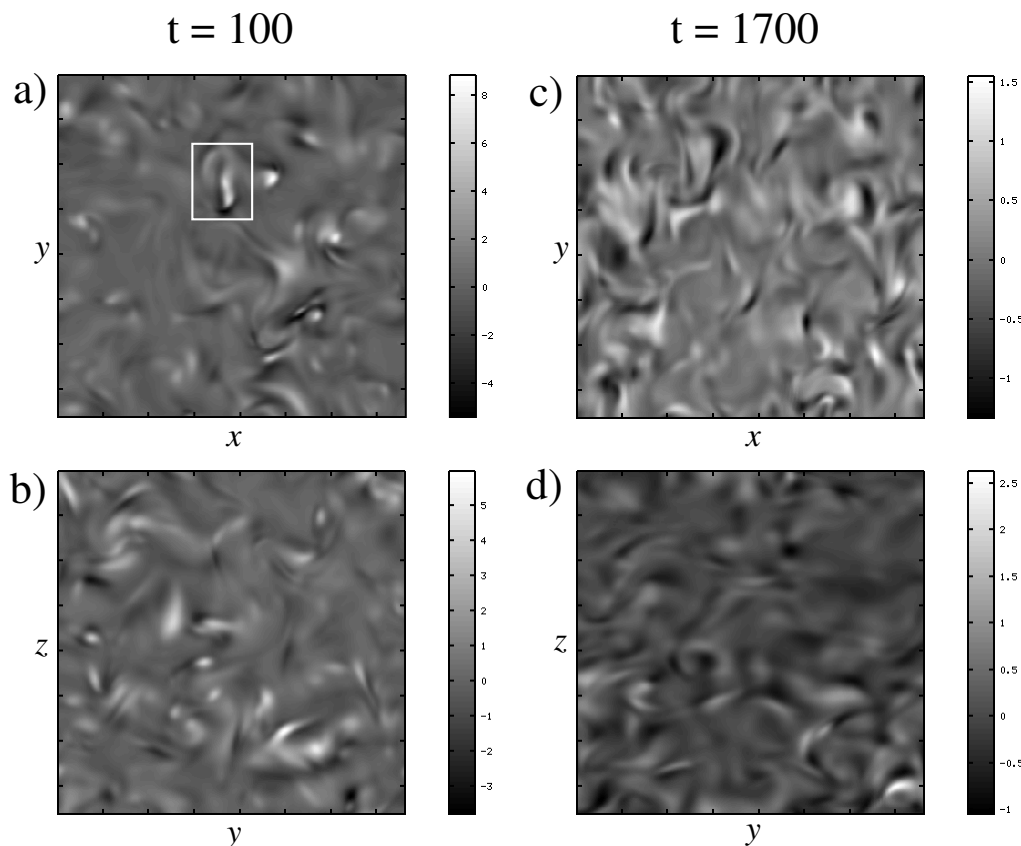


FIGURE 5. Eulerian coherent structures in the velocity field, detected by the Q -criterion at $t = 100$ (left panel) and $t = 1700$ (right panel).

In Fig. 5, intensity plots of the Q -criterion are shown for two-dimensional slices of the box at planes $z = 0$ (upper panels) and $x = 0$ (lower panels) at times $t = 100$ (left panels) and $t = 1700$ (right panels), respectively. Coherent structures with strong vorticity are observed as bright spots, such as the one highlighted by a box in Fig. 5(a). Notice that at $t = 1700$ a large number of bright spots is seen in the xy -plane, but they are rare in the yz -plane, revealing a preferential alignment of coherent structures in the vertical direction in the saturated regime. A similar plot is shown for the magnetic field in Fig. 6, where some of the same coherent structures found in the velocity field can be observed, reflecting the strong coupling between \mathbf{B} and \mathbf{u} in Eqs. (2.2) and (2.3).

Although some coherent structures are clearly detected by this Eulerian technique, the Q -criterion relies on a user defined threshold to determine their boundaries. In order to precisely identify the boundaries and the main transport barriers in the flow, the next section proceeds with a Lagrangian analysis.

3.3. Lagrangian coherent structures

This section describes two tools that can be employed to define/detect coherent structures in the Lagrangian frame, the finite-time Lyapunov exponents and the recently proposed function M .

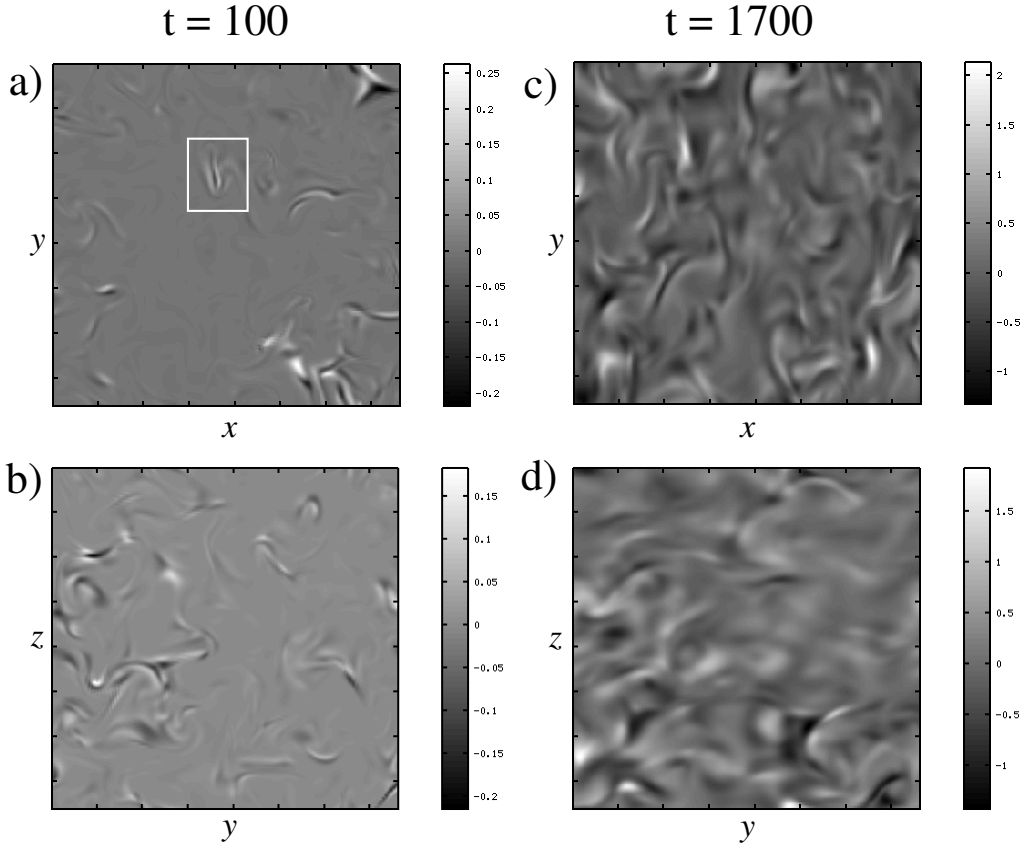


FIGURE 6. Eulerian coherent structures in the magnetic field, detected by the Q -criterion at $t = 100$ (left panel) and $t = 1700$ (right panel).

3.3.1. Finite-time Lyapunov exponents

In the Lagrangian point of view, coherent structures are seen as material surfaces around which trajectory patterns are formed. In Haller & Yuan (2000), these surfaces are simply called Lagrangian coherent structures and are distinguished from other material surfaces in that a LCS exhibits locally the strongest attraction, repulsion or shearing in the flow. Repelling LCSs are responsible for generating stretching, attracting LCSs for folding, and shear LCSs for swirling and jet-type tracer patterns (Haller 2011).

Attracting LCSs have commonly been associated with local maximizing curves (*ridges*) in the backward-time finite-time Lyapunov exponent (FTLE) field and repelling LCSs to ridges in the forward-time FTLE field (Shadden *et al.* 2005; Green *et al.* 2007; Beron-Vera & Olascoaga 2010). There are limitations in such definition, as pointed out by Haller (2011) and Farazmand & Haller (2012), e. g., a ridge in the FTLE field may indicate the presence of a shear LCS or no LCS at all. But in general, ridges in the FTLE fields provide a good approximation to the true LCSs of the flow.

Let $D \subset \mathbb{R}^3$ be the domain of the fluid to be studied, let $\mathbf{x}(t_0) \in D$ denote the position of a passive particle at time t_0 and let $\mathbf{u}(\mathbf{x}, t)$ be the velocity field defined on D . The motion of the particle is given by the solution of the initial value problem

$$\frac{d\mathbf{x}}{dt} = \mathbf{u}(\mathbf{x}(t), t), \quad \mathbf{x}(t_0) = \mathbf{x}_0. \quad (3.3)$$

Let the flow map for \mathbf{u} be defined as $\phi_{t_0}^{t_0+\tau} : \mathbf{x}(t_0) \mapsto \mathbf{x}(t_0+\tau)$. The deformation gradient is given by $J = d\phi_{t_0}^{t_0+\tau}(\mathbf{x})/d\mathbf{x}$ and the finite-time right Cauchy-Green deformation tensor is given by $\Delta = J^T J$. Let $\lambda_1 > \lambda_2 > \lambda_3$ be the eigenvalues of Δ . Then, the finite-time Lyapunov exponents or direct Lyapunov exponents of the trajectory of the particle are defined as

$$\sigma_i^{t_0+\tau}(\mathbf{x}) = \frac{1}{|\tau|} \ln \sqrt{\lambda_i}, \quad i = 1, 2, 3. \quad (3.4)$$

A positive σ_1 is the signature of chaotic streamlines in the velocity field, being a measure of the stretching of fluid elements (although it also incorporates shear (Haller 2011)). In this work, the deformation gradient is computed with second order centered finite-differences.

3.3.2. Function M

Madrid & Mancho (2009) proposed a function to define “distinguished trajectories” (DTs), which are a generalization of the concept of fixed points for aperiodically time-dependent flows. In stationary flows, hyperbolic fixed points are responsible for particle dispersion and nonhyperbolic fixed points for particle confinement. Invariant stable and unstable manifolds of hyperbolic fixed points are barriers to transport and divide the phase space in regions with qualitatively different behaviors. The proposed function, named *function M*, can reveal both hyperbolic and nonhyperbolic flow regions of time-dependent flows. Moreover, M is also useful to detect the stable and unstable manifolds of distinguished hyperbolic trajectories (DHTs), defined as the set of points such that trajectories passing through these points at $t = t_0$ will approach the DHTs at an exponential rate as time goes to infinity or minus infinity, respectively (Branicki *et al.* 2011). The stable and unstable manifolds of DHTs correspond to the repelling and attracting Lagrangian coherent structures, respectively, as defined in the section 3.3.1.

Consider the system given by Eq. (3.3), where $\mathbf{x} = \{x_1, x_2, x_3\}$. For all initial conditions \mathbf{x}_0 in D at a given time t_0 , let us define the function $M(\mathbf{x}_0, t_0) : (D, t) \rightarrow \mathbb{R}$ as

$$M(\mathbf{x}_0, t_0)_\tau = \int_{t_0-\tau}^{t_0+\tau} \left(\sum_{i=1}^3 (dx_i(t)/dt)^2 \right)^{1/2} dt. \quad (3.5)$$

Thus, the function M is a measure of the arc length of the curve traced by \mathbf{x}_0 . Local minima of M represent trajectories that “move less”, being related either to hyperbolic or nonhyperbolic DTs. The manifolds of DHTs are also visible in the M field, since one expects a sharp distinction in the lengths of trajectory curves for particles in regions with different behaviors, separated by stable and unstable manifolds, as noted by Mendoza & Mancho (2010). The technique has been successfully applied to the detection of DTs and manifolds in oceanic (Mendoza & Mancho 2010; Mendoza *et al.* 2010) and stratospheric (de la Cámara *et al.* 2012) flows.

3.3.3. Velocity field structures and chaotic mixing

The FTLEs are computed from a series of fully 3D snapshots of the velocity field taken at different times from t_0 to $t_0 + \tau$. Linear interpolation in time and third-order splines in space are used to obtain the continuous vector fields necessary to obtain the particle trajectories. Figure 7 depicts the probability distribution functions (PDFs) of the three FTLEs at $t_0 = 100$ (left) and $t_0 = 1700$ (right) computed for 64^3 particle trajectories from Eq. (3.4) with a value of τ corresponding to 9 turnover time units, where $u_{rms} \sim 0.28$ for the kinematic phase and $u_{rms} \sim 0.18$ for the saturated regime.

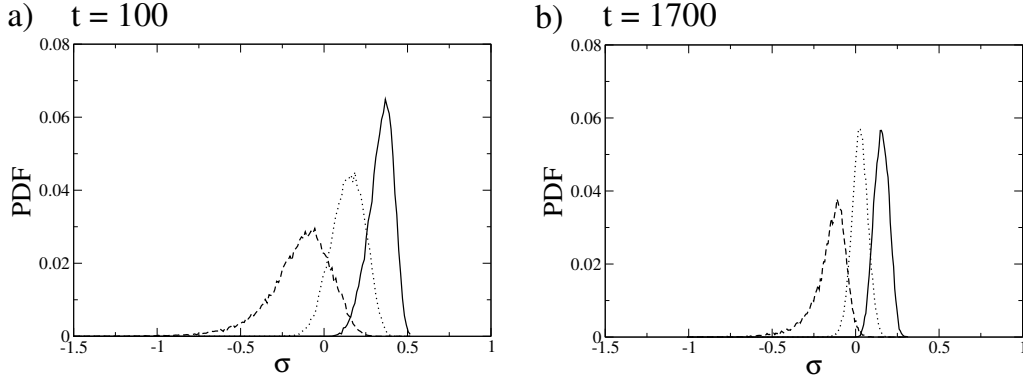


FIGURE 7. Probability density functions (PDFs) of the FTLEs of the velocity field at the kinematic ($t = 100$, left panel) and saturated ($t = 1700$, right panel) regimes. The solid line represents σ_1 , the dotted line, σ_2 , and the dashed line, σ_3 .

Therefore, $\tau = 9/(k_f u_{rms}) \sim 6.4$ time units for the kinematic phase and $\tau \sim 10$ time units for the saturated phase. One can see a clear reduction of Lagrangian chaos in the velocity field at $t_0 = 1700$, with the PDF of σ_1 being shrunk and shifted to the left. There are also fewer regions with two or three positive exponents. Overall, chaotic mixing is diminished due to the growth of B_{rms} and the action of the Lorentz force. The asymmetry in the distributions is typical of heterogeneous mixing, where both regular and irregular trajectories coexist (in finite-time), which means that trajectories cannot uniformly sample the phase space (see, e. g., Beron-Vera & Olascoaga (2010)).

From Fig. 7 it is clear that most trajectories display two positive Lyapunov exponents. Zel'dovich *et al.* (1984) and Chertkov *et al.* (1999) state that in such a case, the total magnetic energy in a kinematic dynamo should behave as $B^2 \propto \exp[(\sigma_1 - \sigma_2)t]$, therefore, one has for the growth rate

$$\gamma = \frac{d \ln \langle B^2 \rangle^{1/2}}{dt} = \frac{d \ln \{\exp[(\sigma_1 - \sigma_2)t/2]\}}{dt} = \frac{\sigma_1 - \sigma_2}{2}. \quad (3.6)$$

At $t_0 = 100$, $\langle \sigma_1 \rangle \sim 0.339$ and $\langle \sigma_2 \rangle \sim 0.143$, which from Eq. (3.6) provides $\gamma = 0.098$ (or $\gamma = 0.07$ in dimensional units), which agrees to within an order of magnitude with the fitted value $\gamma \sim 0.064$, given in Fig. 1.

The remainder of this paper focuses on the backward-time maximum FTLE field, since they reveal the attracting LCSs, which correspond to structures seen using flow visualization in experiments (Green *et al.* 2007). Figure 8 shows the backward-time maximum FTLE field computed for τ corresponding to 9 turnover time units at $t_0 = 100$ (left) and $t_0 = 1700$ (right) from a grid of initial conditions with 512×512 particles. The bright lines represent the attracting LCSs. While the LCSs at $t_0 = 100$ reveal no preferred direction, consistent with an isotropic forcing, at $t_0 = 1700$ there is a clear vertical alignment of LCSs in the xy -slice (Fig. 8(b)). This is due to the super-equipartition magnetic field at $t_0 = 1700$, which develops a large-scale vertical pattern in this plane (see Fig. 2), affecting the alignment of velocity field vectors.

A comparison between Figs. 5 and 8 shows that the FTLE field provides a clearer depiction of coherent structures, with finer details and more precise detection of structure boundaries. Moreover, some coherent structures are only apparent in the FTLE field, such as the large eddy indicated in Fig. 8(d).

From our experience, one of the problems with FTLE plots in turbulent flows is that

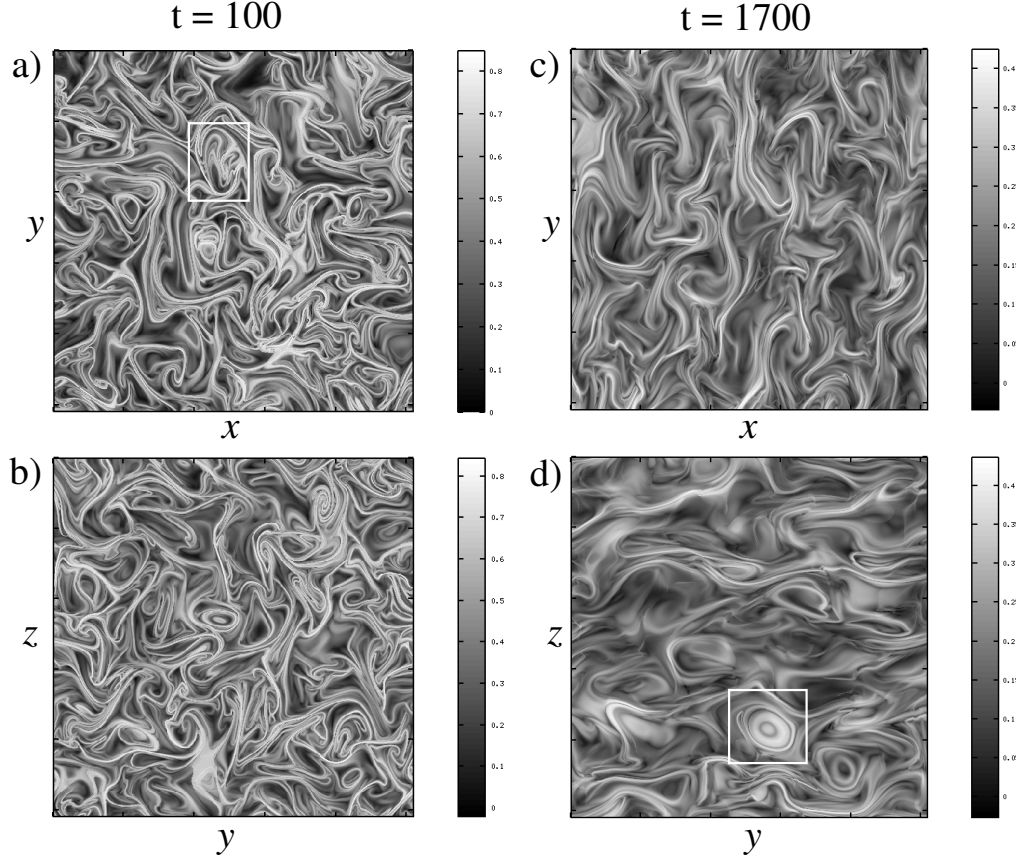


FIGURE 8. Attracting Lagrangian coherent structures in the velocity field, given by the backward-time FTLE at $t_0 = 100$ (left panel) and $t_0 = 1700$ (right panel).

pictures usually become increasingly complex for larger τ , with material lines “growing” and filling the entire phase space. In that sense, it is easier to use function M to detect the main coherent structures of the flow. Figure 9 is a plot of function M with $\tau = 9$ in turnover time units, equivalent to Fig. 8. For the kinematic phase at $t_0 = 100$ (left panel) the eddies are clearly identified as closed regions with distinguished shades of gray. At $t_0 = 1700$ (right panel) the borders between regions are not so sharp and there are wide smooth regions in the flow. Smoothness in the M field indicates that trajectories in those regions do not reach nearby hyperbolic regions during $\pm\tau$ turnover time units, since hyperbolic trajectories are the ones responsible for dispersion and for producing sharp changes in M (Mendoza & Mancho 2010). For larger τ , the boundaries become sharper and more foldings of manifolds are seen, but we keep $\tau = 9$ in all our pictures to facilitate the comparison between both methods in different regimes. Overall, the function M seems to be less sensitive to the choice of τ than the FTLE. Figure 9 corroborates with Fig. 7 in revealing that there is less chaotic mixing after the nonlinear saturation of B_{rms} .

3.3.4. Magnetic field structures and transport of field lines

Our simulations reveal that the magnetic field displays smooth and complex regions (see Fig. 6). If one applies the Lagrangian techniques discussed in the previous section to the magnetic field, the identification of magnetic LCSs provides the main barriers to the

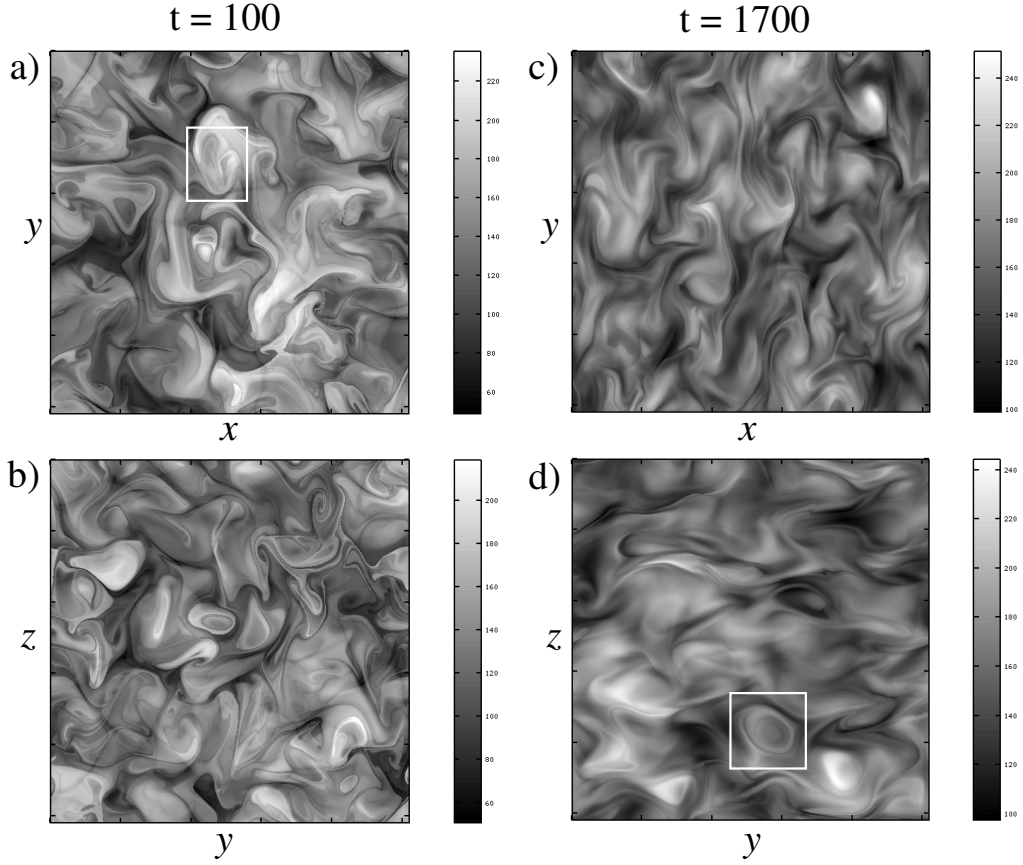


FIGURE 9. Lagrangian coherent structures in the velocity field, given by the function M at $t_0 = 100$ (left panel) and $t_0 = 1700$ (right panel).

transport of field lines, a topic of great interest in magnetic reconnection studies (Evans *et al.* 2004; Grasso *et al.* 2010; Borgogno *et al.* 2011; Yeates & Hornig 2011).

To obtain the magnetic LCSs, the magnetic field at a fixed dynamic time t_0 is used and the maximum FTLE field is computed by integrating

$$\frac{d\mathbf{x}}{ds} = \mathbf{B}(\mathbf{x}(s), t_0), \quad \mathbf{x}(s_0) = \mathbf{x}_0, \quad (3.7)$$

where the parameter (position) s along the field line is seen as an effective time, or field–line–time (Borgogno *et al.* 2011). The flow map for \mathbf{B} is defined as $\phi_{s_0}^{s_0+\tau} : \mathbf{x}(s_0) \rightarrow \mathbf{x}(s_0 + \tau)$. Equation (3.7) is integrated from s_0 to $s_0 + \tau$ with t fixed at t_0 . Lagrangian chaos in the magnetic field is responsible for the transport of magnetic field lines between different regions of the box. Here, the term “transport” is used to refer to motion of field lines in field–line–time, not in dynamic time. Therefore, the maximum FTLE provides a measure of the exponential separation between two neighboring field lines after a finite field–line–time τ , i. e., after a finite distance along the field line.

Figure 10 shows the backward–time maximum FTLE field for the kinematic (left panel) and saturated (right panel) regimes. The high–intensity lines represent attracting magnetic LCSs which act as barriers to field line transport. No transport of magnetic field lines occurs across invariant LCSs and large–scale transport is possible only through

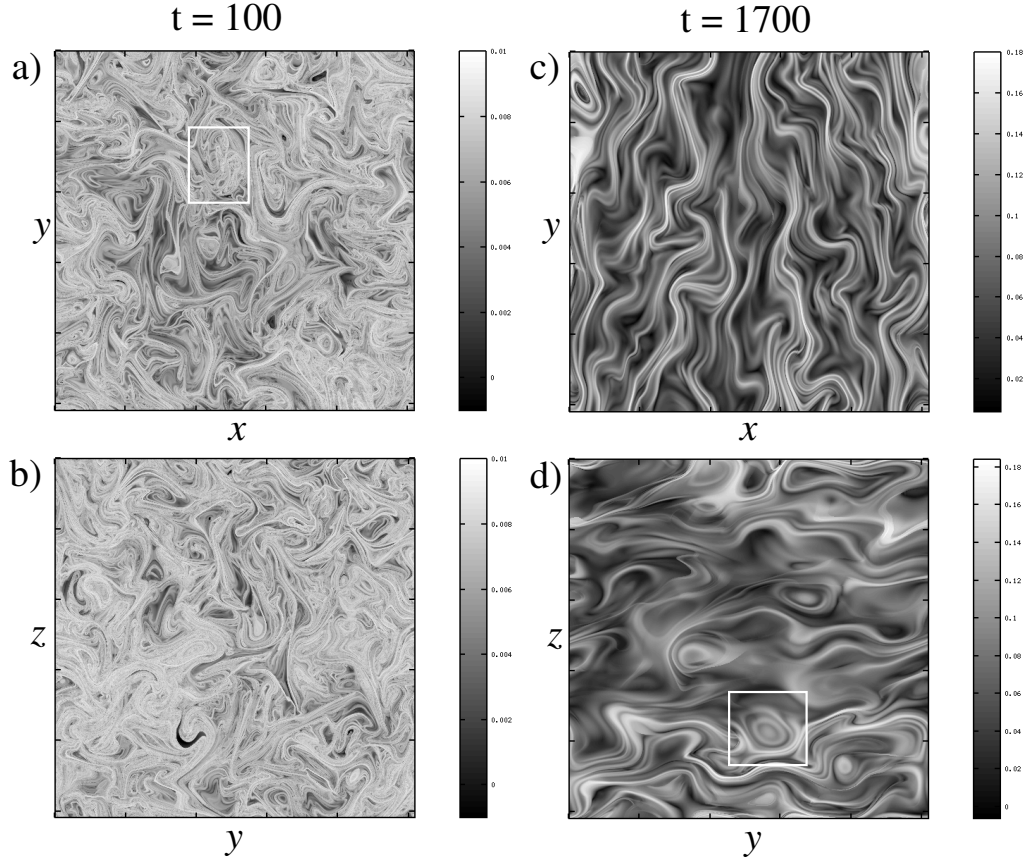


FIGURE 10. Attracting Lagrangian coherent structures in the magnetic field, given by the backward-time maximum FTLE at $t = 100$ (left panel) and $t = 1700$ (right panel).

homoclinic and heteroclinic crossings of attracting and repelling LCSs, where a lobe dynamics mechanism takes place (Grasso *et al.* 2010; Borgogno *et al.* 2011; Yeates & Hornig 2011; Rempel *et al.* 2012). Both FTLE fields are obtained by fixing the evolution (dynamic) time ($t_0 = 100$ for the left panel and $t_0 = 1700$ for the right panel) and setting $\tau = 9/B_{rms}$, where $B_{rms} = 0.014$ for $t_0 = 100$ and $B_{rms} = 0.37$ for $t_0 = 1700$. In the kinematic regime ($t_0 = 100$) the LCSs display no preferred direction, and randomly fill the simulation box. Note that, at least for this value of τ , it is difficult to identify the coherent structure marked in the box in Fig. 10(a) due to the many foldings of attracting lines. After growth and saturation of B_{rms} ($t_0 = 1700$), the randomness of field line orientation is diminished and there is a preferential direction of alignment of field lines which, as mentioned before, directly affects the velocity field. The growth of B_{rms} is also reflected in the presence of many smooth regions in Figs. 10(c) and (d). Consequently, there is less chaotic mixing of field lines.

Once again, to obtain a clearer picture of magnetic coherent structures, we plot in Fig. 11 the function M for $\tau = 9/B_{rms}$. It is easier to spot coherent structures from this field, such as the one in the box in Fig. 11(a). Function M seems to be better than the FTLE field in highlighting the main transport barriers, filtering out spurious lines that are not so important for mixing (Mendoza & Mancho 2010).

As mentioned before, another feature of function M plots is that they provide both the

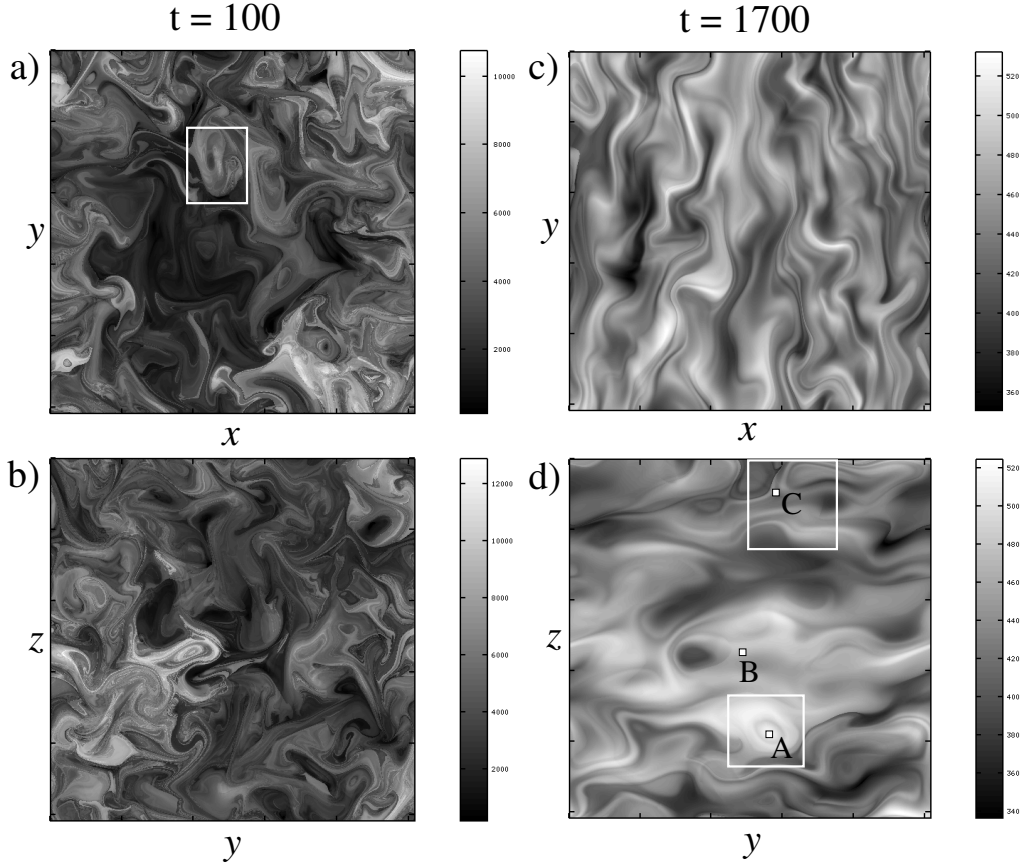


FIGURE 11. Lagrangian coherent structures in the magnetic field, given by the function M at $t = 100$ (left panel) and $t = 1700$ (right panel).

stable and unstable manifolds of DHTs in the same picture. In order to illustrate this feature, three distinct regions are marked in Fig. 11(d). Regions A and B are located in smooth parts of the M field and region C in a region where manifolds are crossing. Smoothness of M in regions A and B indicates that initial conditions in these regions do not perceive nearby hyperbolic regions for $t \in (t_0 - \tau, t_0 + \tau)$ (Mendoza & Mancho 2010). An enlargement of region C is shown in Fig. 12, where the presence of manifolds indicates that field lines in this region either were dispersed in $t_0 - \tau$ or will disperse in $t_0 + \tau$. We define three sets of initial conditions inside the small white squares A, B and C in Fig. 11(d), with each square containing 25 initial conditions. The result of integrating Eqs. (3.7) with each set of initial conditions for $\tau = 9/B_{rms}$ field-line-time units is shown in Fig. 13. Figures 13(a) and (b) show the trajectories of initial conditions in regions A and B, respectively, where it can be seen that all magnetic field lines stay close to each other, forming a magnetic flux tube that is not dispersed in this field-line-time interval. The apparent discontinuities in field lines are due to the periodic boundary conditions. In Fig. 13(c) the trajectories of initial conditions at region C are shown and one can see that there is great chaotic dispersion of field lines due to the crossings of manifolds in this region.

We conclude that function M can efficiently detect transport barriers and dispersion regions in a magnetic field.

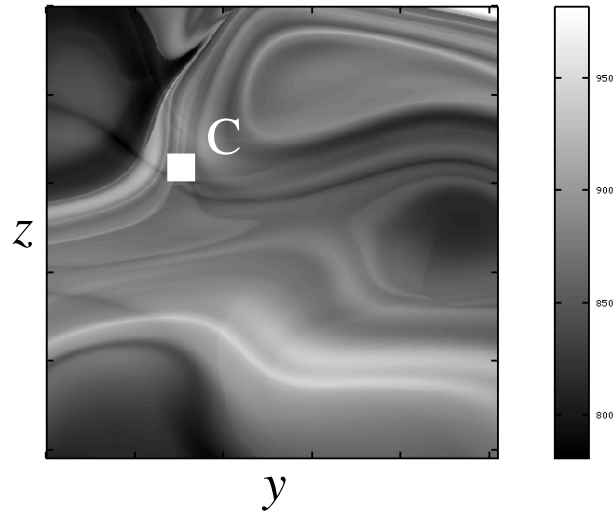


FIGURE 12. Enlargement of the upper rectangle in Fig. 11(d).

$t = 1700$

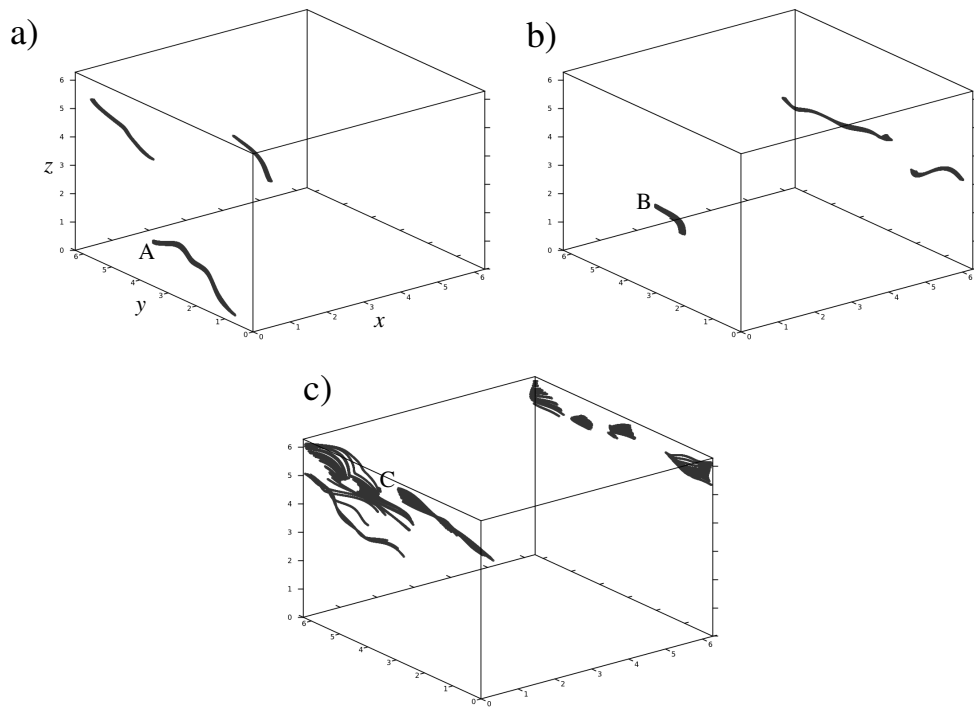


FIGURE 13. Magnetic field lines produced by advecting a small blob of initial conditions in the magnetic field at $t = 1700$. (a) The initial blob is located at A , the point inside a magnetic vortex in Fig. 11(d); (b) the initial blob is located at B , the point in a smooth region of Fig. 11(d); (c) the initial blob is located at C , the point at a crossing of manifolds in Fig. 11(d).

4. Conclusions

Magnetohydrodynamic coherent structures have been identified in direct numerical simulations of a nonlinear dynamo. It was shown that both Eulerian and Lagrangian tools are able to extract vortices from velocity and magnetic field data. Although the Eulerian tool adopted is less computationally expensive, Lagrangian plots show finer details and can better locate the boundaries of vortices. In addition, the Lagrangian analysis provides important information about the mixing properties of the flow. Regarding the numerical tools employed to detect Lagrangian coherent structures (LCSs), the function M seems to be less sensitive to the choice of the integration time τ in comparison to the maximum finite-time Lyapunov exponent (FTLE). Thus, pictures obtained with the FTLE can become increasingly “noisy” with increasing τ due to the complex folding of material lines. Although function M provides “cleaner” pictures, the manifolds (transport barriers) are often not as clearly traced as in a FTLE field. Both tools reveal the strong impact of the magnetic field on the mixing properties of the velocity field when the system moves from the kinematic to the saturated dynamo phases. After the appearance of a strong mean-field, the kinetic and magnetic coherent structures are shown to align in a preferred direction, revealing the anisotropy developed in the vector fields.

Function M is also shown to be useful to detect manifolds of hyperbolic trajectories in the magnetic field, where intense transport of magnetic field lines takes place, a feature that can be further explored to study magnetic reconnection phenomena in plasmas. In relation to this, Lagrangian coherent structures in photospheric velocity fields have been shown to be associated with quasi-separatrix layers in the magnetic field (Yeates *et al.* 2012), which are regions of strong gradients in stretching and squashing of magnetic flux tubes, being identified as the preferential regions for magnetic reconnection (Démoulin 2006; Santos *et al.* 2008). Magnetic reconnection is an important phenomenon in non-linear dynamos, since it is believed that it can reduce the backreaction of the Lorentz force on the velocity field (Blackman 1996). Essentially, turbulent motions can cause the stretching, twisting and folding of weak magnetic field lines in such a way as to produce the growth of magnetic flux. After the magnetic field reaches equipartition with the velocity field, the field lines can restrict fluid motions and transport of material is significantly reduced. This suppression of motions may also inhibit the dynamo. However, if there is rapid reconnection between magnetic flux tubes, this could prevent the tube from backreacting. For other works on the role of magnetic reconnection in dynamo models, see Archontis *et al.* (2003) and Baggaley *et al.* (2009).

We acknowledge Prof. R. A. Miranda, of the University of Brasilia, for his support with numerical codes. E. L. R. acknowledges the support of FAPESP (Brazil), CNPq (Brazil) and NORDITA (Sweden). A. C.-L. C. acknowledges support from CNPq (Brazil), the award of a Marie Curie International Incoming Fellowship and the hospitality of Paris Observatory. P. R. M. acknowledges the support of FAPESP (Brazil).

REFERENCES

- Archontis, V., Dorch, S. B. F. & Nordlund, A. 2003 Numerical simulations of kinematic dynamo action. *Astron. Astrophys.* **397**, 393–399.
- Baggaley, A. W., Barenghi, C. F., Shukurov, A. & Subramanian, K. 2009 Reconnecting flux-rope dynamo. *Phys. Rev. E* **80**, 055301.
- Beron-Vera, F. J. & Olascoaga, M. J. 2010 Surface ocean mixing inferred from different multi-satellite altimetry measurements. *J. Phys. Oceanogr.* **40**, 2466–2480.
- Blackman, E. G. 1996 Overcoming the backreaction on turbulent motions in the presence of magnetic fields. *Phys. Rev. Lett.* **77**, 2694–2697.
- Borgogno, D., Grasso, D., Pegoraro, F. & Schep, T. J. 2011 Barriers in the transition to global

- chaos in collisionless magnetic reconnection. I. Ridges on the finite time Lyapunov exponent field. *Phys. Plasmas* **18**, 102307.
- Brandenburg, A. 2001 The inverse cascade and nonlinear alpha-effect in simulations of isotropic helical hydromagnetic turbulence. *Astrophys. J.* **550**, 824–840.
- Brandenburg, A. & Subramanian, K. 2005 Astrophysical magnetic fields and nonlinear dynamo theory. *Phys. Rep.* **417**, 1–209.
- Brandenburg, A., Klapper, I. & Kurths, J. 1995 Generalized entropies in a turbulent dynamo simulation. *Phys. Rev. E* **52**, R4602–R4605.
- Brandenburg, A., Jennings, R. L., Nordlund, A., Rieutord, M., Stein, R. F. & Tuominen, I. 1996 Magnetic structures in a dynamo simulation *J. Fluid Mech.* **306**, 325–352.
- Branicki, M., Mancho, A. M., Wiggins, S. 2011 A Lagrangian description of transport associated with a fronteddy interaction: Application to data from the North-Western Mediterranean sea. *Physica D.* **240**, 282–304.
- Cattaneo, F., Hughes, D. W. & Kim, E.-J. 1996 Suppression of chaos in a simplified nonlinear dynamo model. *Phys. Rev. Lett.* **76**, 2057–2060.
- de la Cámara, A., Mancho, A. M., Ide, K., Serrano, E. & Mechoso, C. R. 2012 Routes of transport across the Antarctic polar vortex in the southern spring. *J. Atmospheric Sci.* **69**, 741–752.
- Chakraborty, P., Balachandar, S. & Adrian, R. J. 2005 On the relationships between local vortex identification schemes. *J. Fluid Mech.* **535**, 189–214.
- Chertkov, M., Falkovich, G., Kolokolov, I. & Vergassola, M. 1999 Small-scale turbulent dynamo. *Phys. Rev. Lett.* **83**, 4065–4068.
- Chong, M. S., Perry, A. E. & Cantwell, B. J. 1990 A general classification of three-dimensional flow fields. *Phys. Fluids A* **2**, 765–777.
- Démoulin, P. 2006 Extending the concept of separatrices to QSLs for magnetic reconnection. *Adv. Space Res.* **37**, 1269–1282.
- Evans, T. E., Roeder, R. K. W., Carter, J. A. & Rapoport, B. I. 2004 Homoclinic tangles, bifurcations and edge stochasticity in diverted tokamaks. *Contrib. Plasma Phys.* **44**, 235–240.
- Farazmand, M. & Haller, G. 2012 Computing Lagrangian coherent structures from their variational theory. *CHAOS.* **22**, 013128.
- Grasso, D., Borgogno, D., Pegoraro, F. & Schep, T. J. 2010 Barriers to old line transport in 3D magnetic configurations. *J. Physics Conference Series* **260**, 012012.
- Green, M. A., Rowley, C. W. & Haller, G. 2007 Detection of Lagrangian coherent structures in three-dimensional turbulence. *J. Fluid Mech.* **572**, 111–120.
- Haller, G. 2001 Distinguished material surfaces and coherent structures in three-dimensional fluid flows. *Physica D* **149**, 248–277.
- Haller, G. 2005 An objective definition of a vortex. *J. Fluid Mech.* **525**, 1–26.
- Haller, G. 2011 A variational theory of hyperbolic Lagrangian coherent structures. *Physica D.* **240**, 574–598.
- Haller, G. & Yuan, G. 2000 Lagrangian coherent structures and mixing in two-dimensional turbulence. *Physica D.* **147**, 352–370.
- Hunt, J. C. R., Wray, A. A. & Moin, P. 1988 Eddies, streams, and convergence zones in turbulent flows. *Center for Turbulent Research Report* CTR-S88.
- Jeong, J. & Hussain, F. 1995 On the identification of a vortex. *J. Fluid Mech.* **285**, 69–94.
- Lawson, S. J. & Barakos, G. N. 2010 Computational fluid dynamics analyses of flow over weapons-bay geometries. *J. Aircraft.* **47**, 1605–1623.
- Leoncini, X., Agullo, O., Muraglia, M. & Chandre, C. 2006 From chaos of lines to Lagrangian structures in flux conservative fields. *Eur. Phys. J. B* **53**, 351–360.
- Madrid, J. A. J. & Mancho, A. M. 2009 Distinguished trajectories in time dependent vector fields. *CHAOS.* **19**, 013111.
- Mendoza, C. & Mancho, A. M. 2010 Hidden geometry of ocean flows. *Phys. Rev. Lett.* **105**, 038501.
- Mendoza, C., Mancho, A. M. & Rio, M.-H. 2010 The turnstile mechanism across the Kuroshio current: analysis of dynamics in altimeter velocity fields. *Nonlin. Processes Geophys.* **17**, 103–111.
- Moffatt, H. K. 1978 *Magnetic Field Generation in Electrically Conducting Fluids*. Cambridge Univ. Press, Cambridge.

- Peacock, T. & Dabiri, J. 2010 Introduction to focus issue: Lagrangian coherent structures. *CHAOS* **20**, 017501.
- Rempel, E. L., Chian, A. C.-L. & Brandenburg, A. 2011 Lagrangian coherent structures in nonlinear dynamos. *Astrophys. J. Lett.* **735**, L9.
- Rempel, E. L., Chian, A. C.-L. & Brandenburg, A. 2012 Lagrangian chaos in an ABC–forced nonlinear dynamo. *Phys. Scr.* **86**, 018405.
- Santos, J. C., Büchner, J., Madjarska, M. S. & Alves, M. V. 2008 On the relation between DC current locations and an EUV bright point: A case study. *Astron. Astrophys.* **490**, 345–352.
- Shadden, S. C., Lekien, F. & Marsden, J. E. 2005 Definition and properties of Lagrangian coherent structures from finite–time Lyapunov exponents in two–dimensional aperiodic flows. *Physica D.* **212**, 271–304.
- Varun, A. V., Balasubramanian, K. & Sujith, R. I. 2008 An automated vortex detection scheme using the wavelet transform of the d2 field. *Experiments in Fluids* **45**, 857–868.
- Yeates, A. R. & Hornig, G. 2011 A generalized flux function for three-dimensional magnetic reconnection. *Phys. Plasmas* **18**, 102118.
- Yeates, A. R., Hornig, G. & Welsch, B. T. 2012 Lagrangian coherent structures in photospheric flows and their implications for coronal magnetic structures. *Astron. Astrophys.* **539**, A1.
- Zel’dovich, Ya. B., Ruzmaikin, A. A., Molchanov, S. A. & Sokoloff, D. D. 1984 Kinematic dynamo problem in a linear velocity field. *J. Fluid Mech.* **144**, 1–11.
- Zhong, J., Huang, T. S. & Adrian, R. J. 1998 Extracting 3D vortices in turbulent fluid flow. *IEEE Trans. Pattern Anal. Mach. Intell.* **20**, 193–199.
- Zhou, J., Adrian, R. J., Balachandar, S. & Kendall, T. M. 1999 Mechanisms for generating coherent packets of hairpin vortices in channel flow. *J. Fluid Mech.* **387**, 353–396.
- Zienicke, E., Politano, H. & Pouquet, A. 1998 Variable intensity of Lagrangian chaos in the nonlinear dynamo problem. *Phys. Rev. Lett.* **81**, 4640–4643.